J Mater Sci: Mater Electron (2024) 35:2185

Exploration of electrical and dielectric properties of Ho-substituted SrBa-hexaferrite/Ni-spinel ferrite nanocomposites

B. Ünal[1], A. Baykal[2,8,*], M. A. Almessiere[3,4,*], A. Manikandan[5,6], Y. Slimani[3], and A. Ul-Hamid[7]

[1] Department of Electrical-Electronics Engineering, Istanbul Gelişim University, Cihangir Mah. Şehit Jandarma Komando Er Hakan Öner Sk., Avcılar, Istanbul, Turkey
[2] Food Engineering Department, Faculty of Engineering, Istanbul Aydin University, Florya, Istanbul 34295, Turkey
[3] Department of Biophysics, Institute for Research and Medical Consultations (IRMC), Imam Abdulrahman Bin Faisal University (IAU), P.O. Box 1982, Dammam 31441, Saudi Arabia
[4] Department of Physics, College of Science, Imam Abdulrahman Bin Faisal University (IAU), P.O. Box 1982, Dammam 31441, Saudi Arabia
[5] Department of Chemistry, Karpagam Academy of Higher Education, Coimbatore 641 021, Tamil Nadu, India
[6] Centre for Material Chemistry, Karpagam Academy of Higher Education, Coimbatore 641 021, Tamil Nadu, India
[7] Core Research Facilities, King Fahd University of Petroleum & Minerals, Dhahran 31261, Saudi Arabia
[8] Basic Pharmacy Department, Pharmacy Faculty, Istanbul Aydin University, Istanbul 34295, Turkey

Received: 4 August 2024
Accepted: 13 November 2024
Published online: 29 November 2024

ABSTRACT

Hard/soft $Sr_{0.5}Ba_{0.5}Ho_xFe_{12-x}O_{19}/NiFe_2O_4$ nanocomposites **(H/S Ho-SBF/NFO (x ≤ 0.08) NCs)** have been synthesized via a one-pot sol–gel combustion route. X-ray powder diffraction analysis confirmed the formation of both cubic and hexagonal structures and nano size of all samples. The chemical compositions of the products were followed via Energy Dispersive X-ray spectroscopy (EDX). This study systematically explores the dielectric and electrical properties of **H/S Ho-SBF/NFO (x ≤ 0.08) NCs**, where the Ho^{3+} ion doping ranges from 0.00 to 0.08. Measurements encompassed up to 3.0 MHz and between 20 and 120 °C. The investigation includes an in-depth analysis of *ac/dc* conductivity, dielectric constant, dielectric loss, dissipation factor, and real and imaginary modulus (*ImM*) across the entire range of Ho^{3+} ion substitution ratios. Results demonstrate that conductivity variations exhibit power law dynamics relative to frequency (*f*), predominantly influenced by Ho^{3+} ion substitutions in the NCs. The *f*-dependent behavior of the dielectric constant across all NCs underscores its sensitivity to the substitution ratio “x”, with most dielectric parameters attributed to interactions between grains and grain boundaries. These findings align with conduction mechanisms typical in compositional ferrites, consistent with Koop’s model.

Address correspondence to E-mail: abdulhadibaykal@aydin.edu.tr; malmessiere@iau.edu.sa

https://doi.org/10.1007/s10854-024-13916-3

1 Introduction

Due to their exceptional electric, high electrical resistance, dielectric, temperature (*T*) and corrosion stability, magnetic, structural, coexistence of the insulating, magnetic, and microwave properties, and their potential usage in medicine, cancer treatment, hydrogen production, hydrogen storage, electrochemical hydrogen storage, telecommunication, sensors, data storage, microwave applications, and photocatalysis, magnetic nanomaterials and nanocomposites are important technological materials [1–4]. Composite materials show distinct properties compared to their individual phases and also interface plays an important role in these composites [5–7]. Researchers are turning their attention to composite materials to meet the growing need for sustainable applications of functional materials, as single substances often fall short of fulfilling technological demands in numerous instances [8]. Compared with single-phase ferrite, ferrite nanocomposite has the high coercivity of the hard magnetic phase and high saturation magnetization of the soft magnetic phase, resulting in high magnetic energy product $(BH)_{max}$ of nanocomposites [9].

Mostly magnetic and microwave properties of H/S NCs have been investigated. So, the number of papers based on dielectric and electrical features of H/S NCs is not so high. Mansour et al. [10] synthesized and investigated both the dielectric and microwave properties of H/S BaAlZn hexaferrit/MnMg spinel ferrite NCs. Abarna et al. [11] studied on dielectric and magnetic features of BaSr hexaferrite/$Zn_{0.5}Co_{0.5}$-spinel ferrite NCs. Almessiere et al. [12] investigated the electrical features and reflection losses of H/S (Sr M-type hexaferrite)/x($Ni_{0.8}Zn_{0.2}$-spinel ferrite) nanocomposites. In another study, Almessiere et al. [13] researched the dielectric and electrical features of H/S (Co-spinel ferrite)/(NiSc spinel ferrite)$_x$ NCs. C.C. Chauhan et al. [14] studied the dielectric and magnetic features of H/S $SrFe_{12}O_{19}$/($NiFe_2O_4$ NCs. G.I. Choudhari et al. [15] considered the structural, magnetic, and dielectric features of H/S (100−x)$SrFe_{12}O_{19}$−(x) $CoFe_2O_4$ composites. Almessiere et al. [16] studied the impact of calcination temperatures on the dielectric and electrical properties of H/S SrGa hexaferrite/ZnNi spinel ferrite NCs.

A great variety of experimental methods have been used in the production of nanoferrites, like the solid state techniques, hydrothermal method, auto-combustion method, co-precipitation method, refluxing method, microwave sintering method, spray-spin-heating-coating method, pulsed wire discharge method, etc. Among them, the main advantages of the sol–gel process are the high purity of the product, the narrow particle size distribution, and the achievement of uniform nanostructure at low temperatures [17].

In this work, H/S samples were fabricated via one-pot sol–gel combustion route. As compared with the physical mixing route, sol–gel combustion route is economical, simple, high yield, and particle size and distribution of the material can be easily controlled [11, 18]. The structural, electrical, and dielectric features of the H/S $Sr_{0.5}Ba_{0.5}Ho_xFe_{12-x}O_{19}$/NFO NCs have been investigated in detail for the first time and presented in this study.

2 Experimental

2.1 Chemicals and instrumentations

$Sr(NO_3)_2$ (97%), $Fe(NO_3)_3.9H_2O$ (98%), $Ni(NO_3)_2·6H_2O$ (96%), $Ba(CH_3COO)_2$ (95%), Citric acid ($C_6H_8O_7$) (99.5%), $(NH_4)_6Mo_7O_{24}$ (99%) were obtained from Merck and used as received in synthesis of H/S Ho-SBF/NFO ($x \leq 0.08$) NCs. Rigaku X-ray diffractometer (XRD) has been used to verify the structure of the products. FEI Teneo Scanning (SEM) and FEI Titan Transmission (TEM) electron microscopes were used for the morphological investigation of the products. The electrical measurements were done via the Novocontrol Alpha impedance analyzer.

2.2 Synthesis

The detail of synthesis of **H/S Ho-SBF/NFO (x ≤ 0.08) NCs** has been already reported in previous publication [19].

3 Results and discussion

3.1 Structure and morphology

The structure of H/S Ho-SBF/NFO ($x \leq 0.08$) NCs with varying Ho ratios is presented in Fig. 1a with minor phase of α-Fe_2O_3. The XRD patterns showed both SBFO and NFO phases were overlapping. The lattice parameters and crystallite size of both SBFO and NFO phases ($x \leq 0.08$) NCs are displayed in Fig. 1b, c, and d.

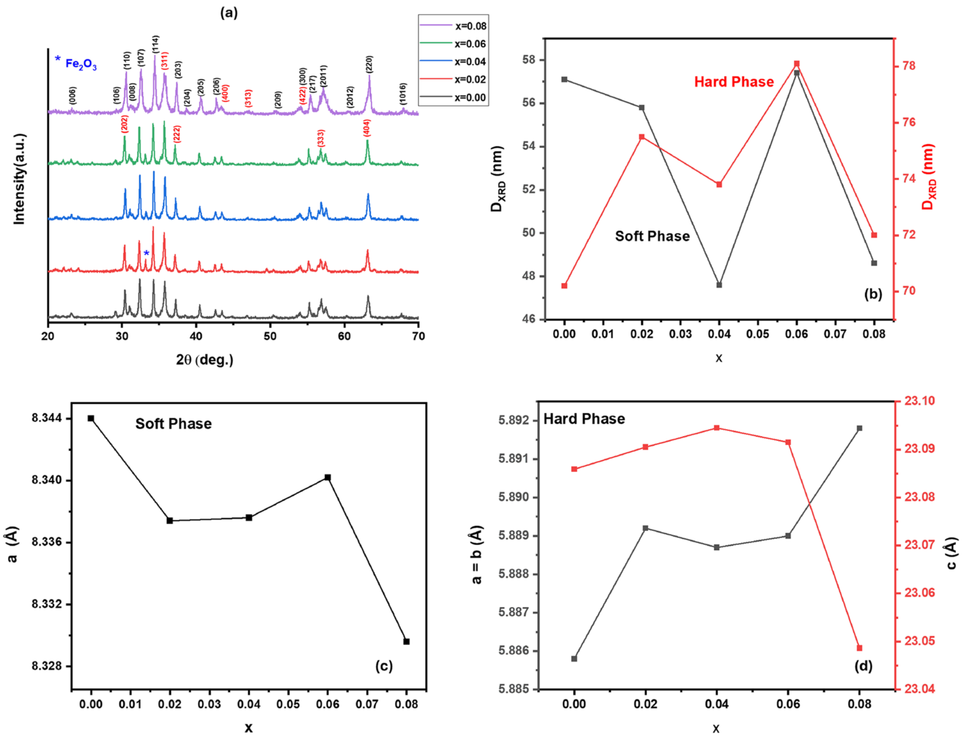

Fig. 1 **a** XRD powder patterns of H/S Ho-SBF/NFO ($x = 0.06$) NCs, **b** crystallite size (D_{XRD}), **c** lattice parameters of soft phase (NFO), and **d** lattice parameters of hard phase (Ho_x-SBFO). Data were reused from [19].

The intensity of the most intense peak in spinel ferrite (311) is increasing as the ratio of Ho increases.

Figure 2 demonstrates the SEM images of (H/S Ho-SBF/NFO ($x = 0.00$, 0.02 and 0.06) NCs. The observed images displayed a highly agglomerated hexagonal and cubic particles [19]. Furthermore, the EDX spectrum of H/S Ho-SBF/NFO ($x = 0.06$) NCs is represented in Fig. 3. The spectrum revealed the chemical compositions of two phases inside the samples. The particle morphology of H/S Ho-SBF/NFO ($x = 0.06$) NCs was distinctly seen utilizing two different magnification TEM images, as illustrated in Fig. 4. The images revealed a cluster of cubic and hexagonal particles.

3.2 Electrical and dielectric properties

Understanding the electrical and dielectric features of nanocomposite materials is crucial for their technological applications. This study examines these properties in H/S $Sr_{0.5}Ba_{0.5}Ho_xFe_{12-x}O_{19}$/NFO NCs, focusing on parameters such as *ac*/*dc* conductivity, dielectric loss-constant, and dissipation factor. The investigation

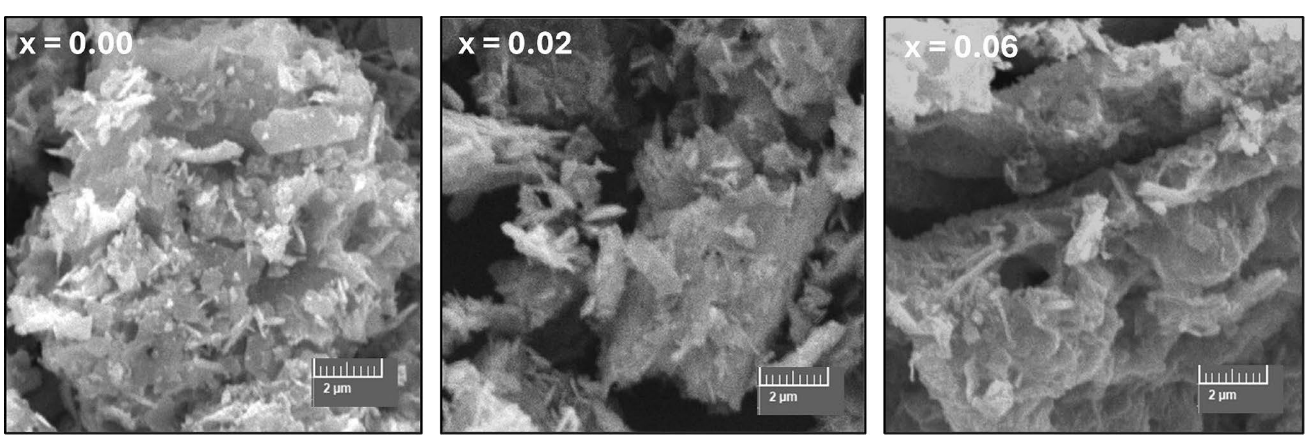

Fig. 2 SEM images of Ho-SBF/NFO NCs ($x = 0.00$, 0.02 and 0.06) NCs

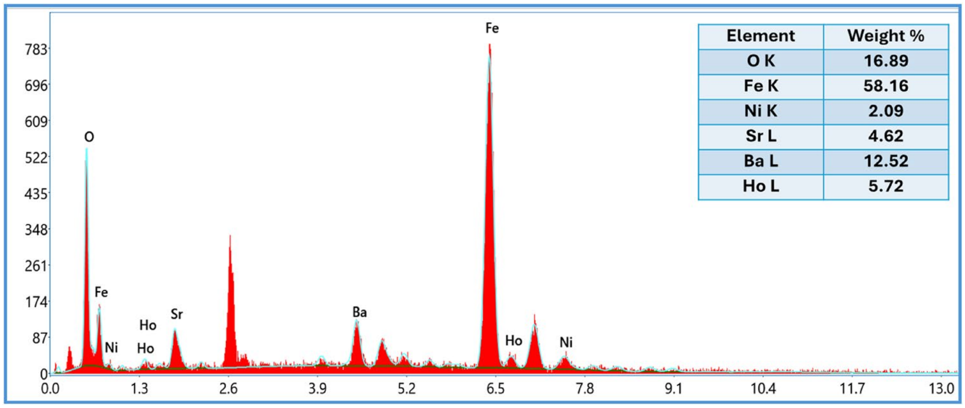

Fig. 3 EDX spectrum of H/S Ho-SBF/NFO ($x = 0.06$) NCs

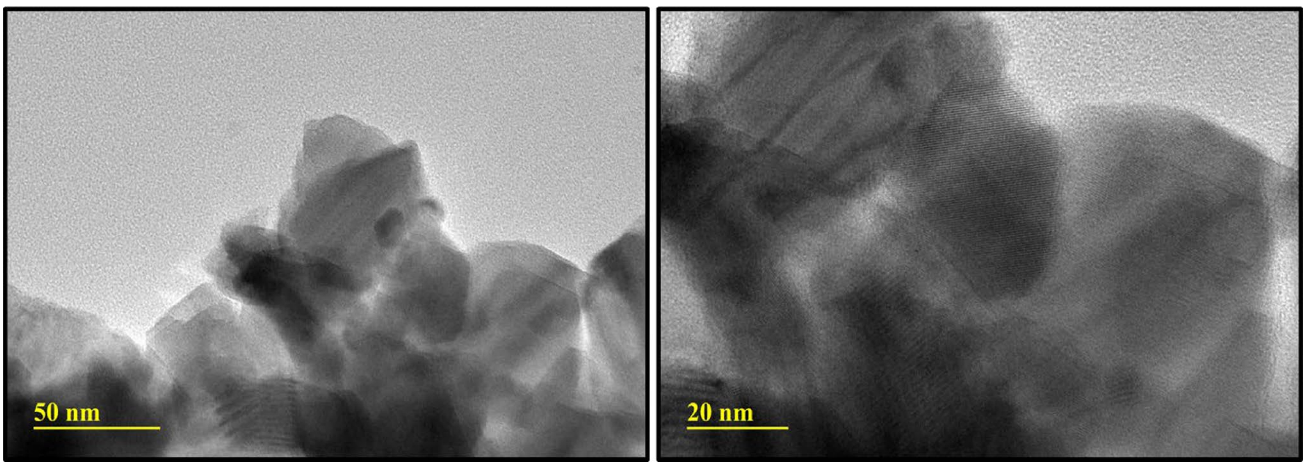

Fig. 4 TEM images of H/S Ho-SBF/NFO ($x = 0.06$) NCs

considers these properties as dependent variables of applied voltage *f* and measurement *T*, considering the different substitution ratios present in the NCs. The analysis covers up to 120 °C and to 3.0 MHz, revealing the detailed electrical and dielectric behaviors under varying environmental conditions.

3.2.1 AC conductivity

Hexaferrites are characterized by a hexagonal crystal structure composed primarily of iron oxides alongside other metal ions. When holmium ions substitute into this structure, they displace some of the iron or other metal ions, profoundly influencing the electronic structure and cation distribution within the NCs. This substitution plays a pivotal role in shaping the electrical properties of the material, particularly in nanocomposites (NCs) involving Ho-ion-substituted BaSr-hexaferrites (HFs) and Ni spinel ferrites (SFs), essential for diverse technological applications. The *ac* conductivity of Ho-ion-substituted hexaferrites exhibits a strong *f* dependence: at low frequencies, conductivity tends to be lower, influenced by grain boundary effects and space charge polarization. As *f* increases, conductivity rises due to enhanced charge carrier hopping. Typically, conductivity follows a power law relationship with *f* ($\sigma_{ac} \propto \omega^s$), ω is the angular *f* and *s* is an exponent less than 1.

In this study, the *ac* conductivity of H/S $Sr_{0.5}Ba_{0.5}Ho_xFe_{12-x}O_{19}$/NFO NCs was investigated across up to 120 °C and to 3.0 MHz, revealing distinct trends dependent on Ho^{3+} ion substitution ratios and environmental conditions (Fig. 5). For $x = 0.00$ NCs, conductivity variations generally conform to the power law across *T*s, with minor deviations noted at specific *f*–*T* intersections. Increasing the substitution ratio from $x = 0.02$ to 0.08 amplifies the peak *ac* conductivity at lower frequencies, underscoring the sensitivity of conductivity to substitution levels. At

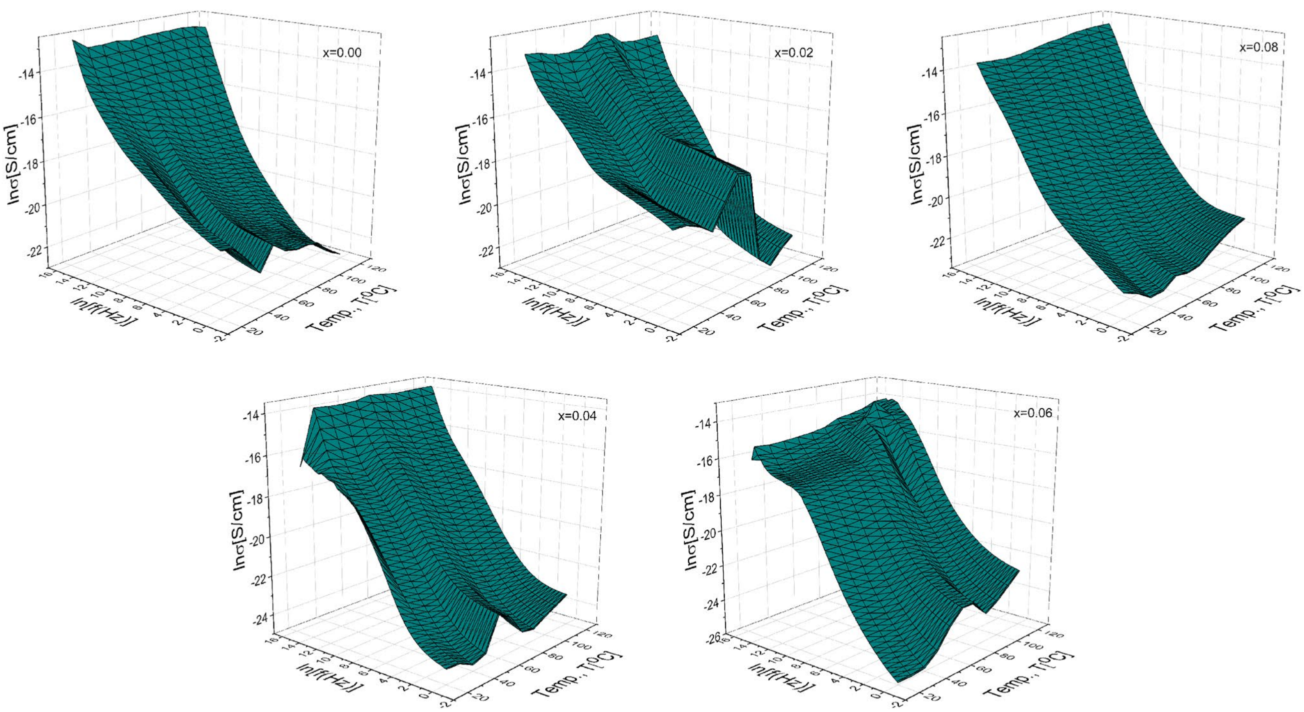

Fig. 5 3D characterization of *ac* conductivity of H/S $Sr_{0.5}Ba_{0.5}Ho_xFe_{12-x}O_{19}$/NFO NCs

$x = 0.08$, conductivity exhibits pronounced yet attenuated T fluctuations, with reduced variability at higher frequencies. Across all NCs, conductivity typically increases with f, demonstrating significant variations over distinct T ranges, particularly noticeable for $x = 0.08$. Structural modifications induced by substitution ratios influence the conduction mechanism, complicating the composite material's behavior. At higher frequencies, NCs exhibit nearly T-independent conductivity across all substitutions.

Conduction mechanisms in these materials arise from interactions between charge carriers and the composite matrix, encompassing intra-grain paths, defects, and grain boundaries [14]. Understanding these mechanisms is crucial for tailoring the electrical properties of NCs for specific applications. Key mechanisms include electronic and ionic conduction facilitated by modified energy bands and introduced ionic species, respectively. Defect-mediated hopping conduction also plays a significant role, providing localized pathways for charge transport. Moreover, polarization effects due to dipole alignment within grains, influenced by holmium's ionic radius and magnetic moment, contribute to AC conductivity. Grain boundaries act as barriers to charge transport, whose characteristics are altered by the presence of holmium ions. This study illuminates the intricate relationships among material composition, T, and f in determining *ac* conductivity in H/S $Sr_{0.5}Ba_{0.5}Ho_xFe_{12-x}O_{19}$/NFO NCs. Understanding these mechanisms provides crucial insights into their electrical behavior, guiding strategies for optimizing conductivity and enhancing functionality across various technological applications.

3.2.2 DC conductivity and activation energy (Ea)

The Arrhenius plot of the *dc* conductivity for H/S $Sr_{0.5}Ba_{0.5}Ho_xFe_{12-x}O_{19}$/NFO NCs up to 120 °C and to 1.0 Hz highlights the significant impact of Ho^{3+} ion substitution ratios on both dc E_a (see Fig. 6). This study investigates how the substitution of Ho ions affects the conduction mechanisms, transitioning between semiconductor-like and metallic-like behaviors. Impact of Ho^{3+} ion substitution is that (i) the Ea varies with Ho substitution ratios and T, indicating a transition between different conduction mechanisms and (ii) At $x = 0.08$, the Ea shows distinct behavior across T variations, suggesting unique interactions between the material's structure and charge carriers [15].

The role of E_a is that (i) E_a represents the energy barrier for charge carrier movement. (ii) Higher E_a

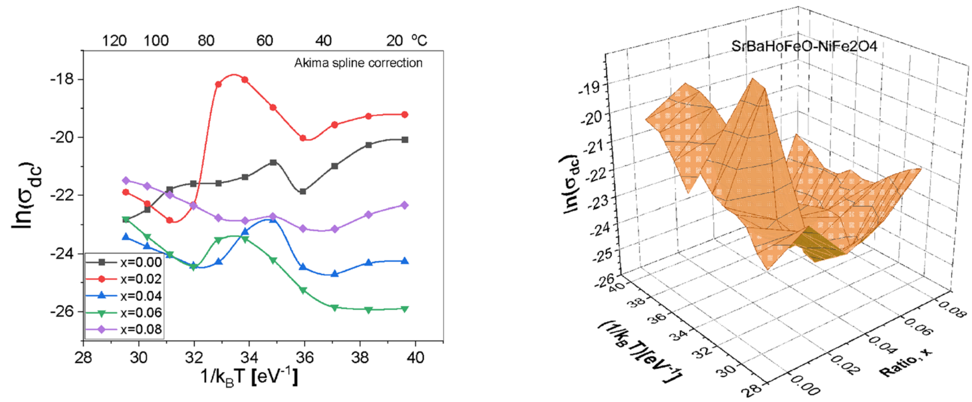

Fig. 6 2D and 3D Arrhenius plotting of *dc* conductivity of H/S $Sr_{0.5}Ba_{0.5}Ho_xFe_{12-x}O_{19}$/NFO NCs

values indicate greater barriers and lower conductivity, while lower E_a values facilitate charge transport and higher conductivity. Mechanisms influencing *dc* conductivity is that charge carrier mobility in which the substitution of Ho^{3+} ions affects the number of free charge carriers and introduces additional energy levels within the band gap. The presence of grain boundaries, crystal structure, and defects influences the mobility of charge carriers. According to the hopping mechanism in the NCs, electrons hop between Fe^{2+} and Fe^{3+} ions. Ho^{3+} ion substitution can alter the concentration and distribution of these ions. Increased T provides more energy to excite electrons into the conduction band or facilitate hopping between localized states. The large ionic radius of Ho^{3+} compared to Fe^{3+} causes local lattice distortions, affecting charge carrier mobility. Ho^{3+} ion introduction can create impurity levels within the band gap, acting as traps or recombination centers. Grain boundaries can act as potential barriers to charge carrier movement. Ho^{3+} ion substitution can alter these barriers, impacting conductivity. At grain boundaries, charge accumulation can create space charge regions that influence charge carrier movement. These measurements provide insights into E_a and charge transport mechanisms within specific substitution ratios. Analyzing *dc* conductivity and E_a in H/S $Sr_{0.5}Ba_{0.5}Ho_xFe_{12-x}O_{19}$/NFO NCs elucidates the relationship between material composition, charge transport mechanisms, and electrical properties. This understanding is crucial for optimizing NC performance in applications such as magnetic storage, microwave devices, or electromagnetic shielding. Tailoring material composition and processing parameters can enhance conductivity and reduce E_a, improving NC functionality across various technological domains [10, 12].

3.2.3 Dielectric constant

The dielectric constant of H/S $Sr_{0.5}Ba_{0.5}Ho_xFe_{12-x}O_{19}$/NFO NCs was investigated across frequencies up to 3.0 MHz and to 120 °C. As depicted in Fig. 7, the dielectric constant generally decreases with increasing f, a trend significantly influenced by the Ho^{3+} ion substitution ratio "x". This relationship exhibits distinctive curvature and fluctuation patterns along the T axis, underscoring the intricate interplay between substitution ratio and dielectric behavior.

T variations yield diverse outcomes for each substitution ratio, particularly notable at $x = 0.08$, where significant curvilinear changes are observed. With rising T, the dielectric constant tends to increase with f, albeit at a diminishing rate. Other substitution ratios also show T-dependent fluctuations in the dielectric constant. These observations can be elucidated through the bilayer model, which posits the role of highly conductive grains at insulating grain boundaries.

At $x = 0.08$, the dielectric constant closely aligns with high f values at elevated Ts, indicating substantial variations in the relationship between grains and grain boundaries. Generally, ferrite structures exhibit reduced f dependence at higher frequencies, with specific substitution ratios exhibiting T-sensitive dielectric constants due to charge exchange between Fe^{3+} and Fe^{2+} ions [20]. Overall, the behavior of the dielectric constant at $x = 0.08$ underscores the profound influence of factors such as charge polarization, measurement T, cation distribution, and structural arrangements on the electrical and dielectric properties of these nanocomposites [21].

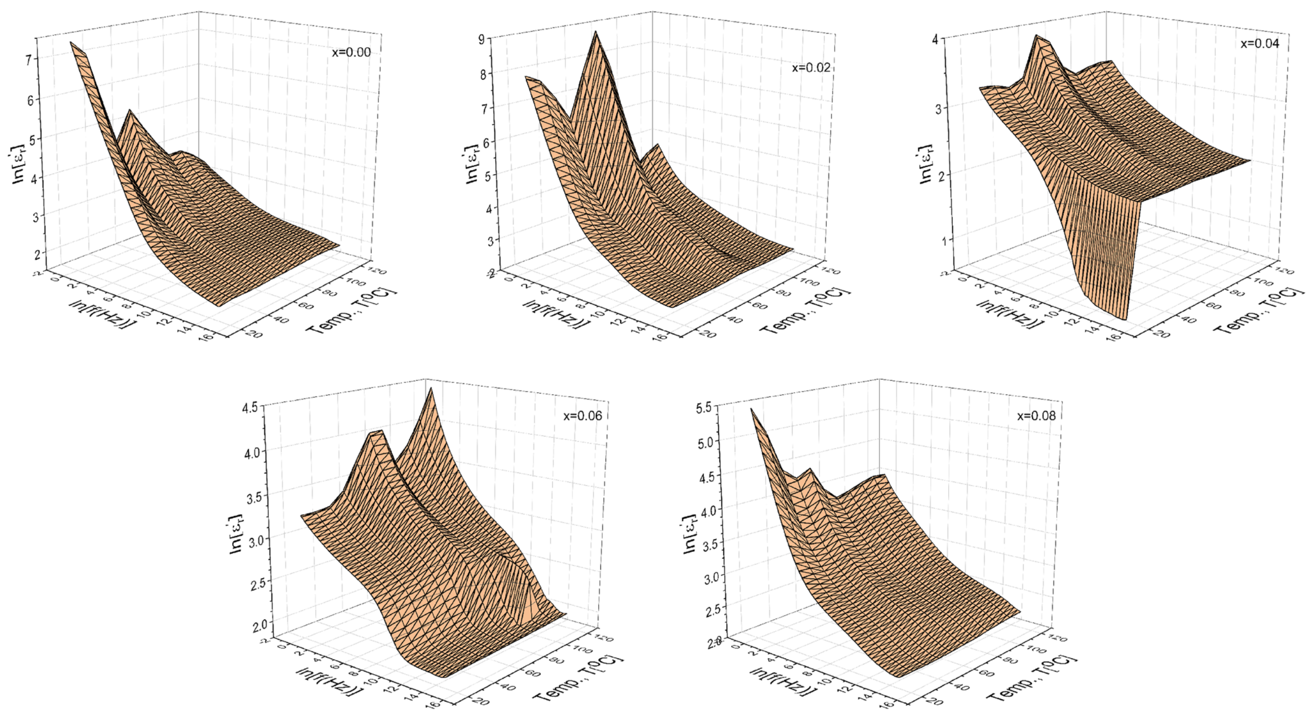

Fig. 7 3D graphical representation of dielectric constant of H/S $Sr_{0.5}Ba_{0.5}Ho_xFe_{12-x}O_{19}$/NFO NCs

3.2.4 Dielectric loss

The dielectric loss of H/S $Sr_{0.5}Ba_{0.5}Ho_xFe_{12-x}O_{19}$/NFO NCs, depicted in a 3D graphical representation in Fig. 8, generally decreases with increasing *f*. However, variations are observed due to substitution effects, particularly notable at $x = 0.06$ where fluctuations occur with increasing *f* and *T* changes outside the $x = 0.08$ ratio. The presence of Ho^{3+} ions exerts a significant influence on dielectric loss. At $x = 0.08$, *T* dependency is evident as increased thermal energy enhances the substitution of Ba^{2+} ions with Fe^{3+} host ions in the NCs, impacting both octahedral (O_h) and tetrahedral (T_d) regions. This behavior is attributed to compositional defects, cation distribution, charge polarization, and thermally stimulated ionic rearrangements affecting charge carrier conduction mechanisms.

The migration of Fe ions from Oh to Td sites due to Ho-ion substitutions increases electrical conductivity while decreasing dielectric constant and loss. Dielectric loss is influenced by the dissipation factor and dielectric constant, both of which vary with *f*, *T*, and substitution ratio. Significant dispersion in dielectric loss is observed for Ho^{3+} ion substitutions at low frequencies, decreasing in the medium and high f regions following a power law dependence. This reduction is associated with the interface relaxation process described by Koop's model [22], where grains conduct more effectively than grain boundaries.

T -induced fluctuations in dielectric loss are noted for all NCs except $x = 0.08$, which exhibits unique behavior. The dependency on *T* and substitution ratio is pronounced, with dielectric loss generally decreasing at higher substitution ratios due to enhanced conduction. Dispersion in dielectric losses is wider at lower frequencies across all NCs, diminishing at higher frequencies due to faster charge displacement within grains influenced by changes in ferrous ion concentrations resulting from substitution ions at Oh sites.

3.2.5 Dissipation factor

The dissipation factor, also known as tangent loss, for H/S $Sr_{0.5}Ba_{0.5}Ho_xFe_{12-x}O_{19}$/NFO NCs is illustrated in Fig. 9 using a 3D graphical representation. At high frequencies, it demonstrates consistent *T* independence across all NCs. In the medium *f* range, there is minimal *T* sensitivity, with slight increases observed for $x = 0.06$ NCs across different *T* s. At low frequencies, significant variations are noted depending on

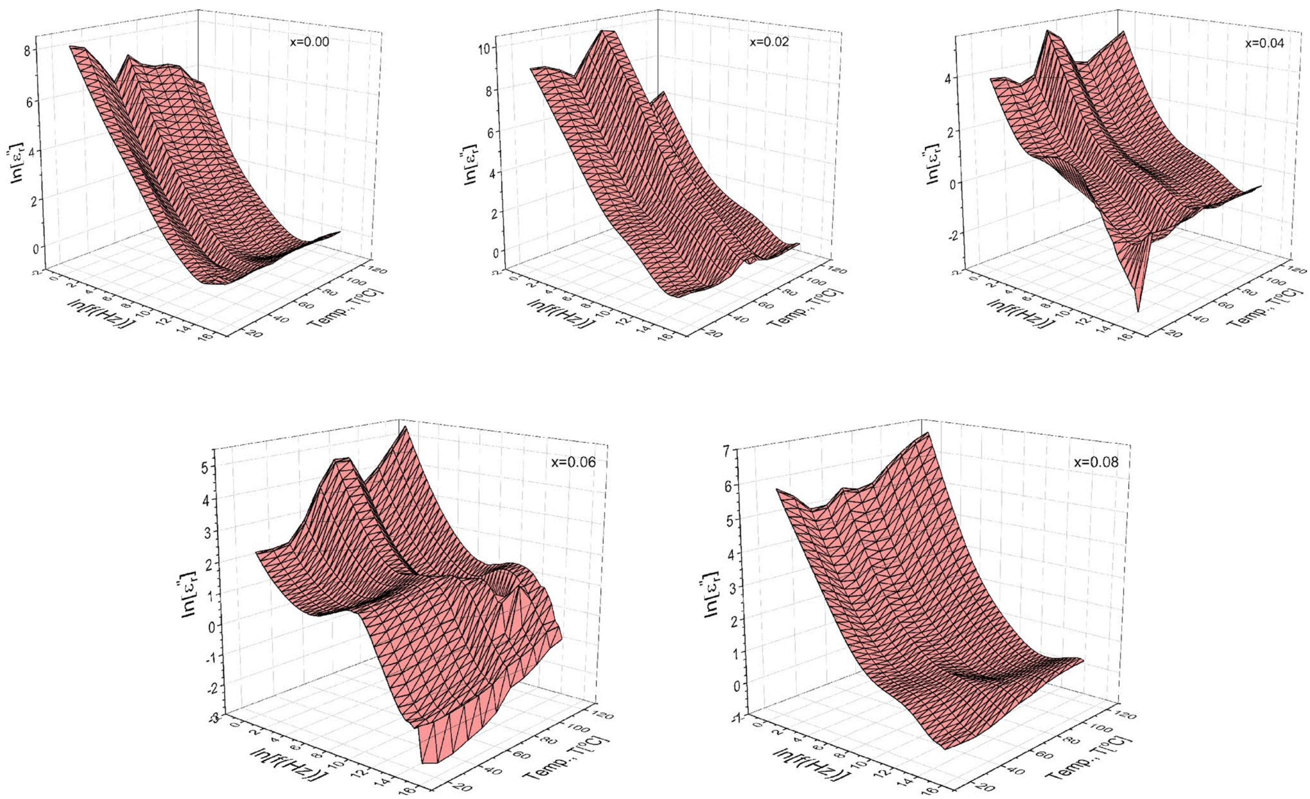

Fig. 8 3D graphical representation of dielectric loss of H/S $Sr_{0.5}Ba_{0.5}Ho_xFe_{12-x}O_{19}$/NFO NCs

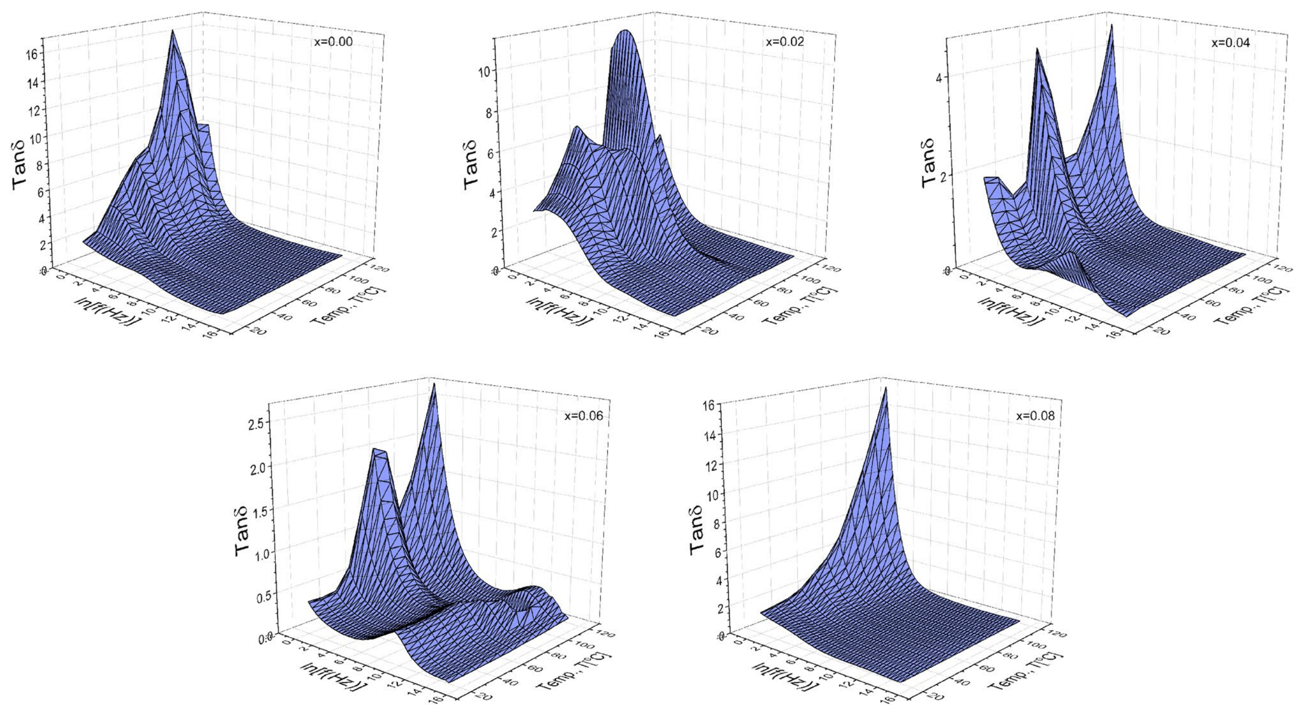

Fig. 9 3D representation of dissipation factor of H/S $Sr_{0.5}Ba_{0.5}Ho_xFe_{12-x}O_{19}$/NFO NCs

the substitution ratio. The highest dissipation factor values occur at the lowest frequencies and highest *T*s for $x = 0.04$, 0.06, and 0.08, with distinct peaks at lower frequencies observed for $x = 0.04$ and 0.06. For $x = 0.08$, a steady increase is observed at low frequencies with increasing *T*, peaking at the highest *T*s. The conduction mechanism is influenced by electron/polaron hopping processes, which are impacted by both *T* and substitution ratios, influenced by the hexa-to-spinel ferrite composition ratio. The dielectric properties of these NCs align with typical conduction mechanisms found in compositional ferrites, as explained by Koop's model [22]. Understanding the dissipation factor's dependence on *T* and *f* is crucial for optimizing electrical and dielectric parameters in applications such as contrast agents, gas sensors, medical devices etc.

3.2.6 Complex dielectric modulus

The complex dielectric modulus serves as a crucial tool for analyzing the dielectric characteristics of ferrite nanocomposites (NCs) and understanding the conduction mechanisms, especially concerning electrode polarization. It allows for the separation into real ($M'(\omega)$) and imaginary ($M''(\omega)$) components derived from complex dielectric data, which are influenced by parameters such as the dielectric constant and dielectric loss. These components vary with *T* and substitution ratio, providing insights into the dielectric behavior of the NCs [2, 23, 24].

3.2.6.1 Real modulus The 3D representation of the real modulus (ReM) for H/S $Sr_{0.5}Ba_{0.5}Ho_xFe_{12-x}O_{19}$/NFO NCs, depicted in Fig. 10, illustrates how ReM correlates with both *f* and *T* across various Ho^{3+} ion substitution ratios between 0.00 and 0.08. This visualization provides insights into the variations of ReM in response to changes in *f* and *T* across different levels of Ho^{3+} ion substitution. Each ReM plot shows distinct dependencies on the substitution ratio concerning *f* and *T* variations. Particularly noteworthy is the significant *T* dependency of ReM at higher frequencies, whereas at lower and medium frequencies, each NC exhibits diverse tendencies in response to *T* changes. For $x = 0.08$ and 0.06 (except in the low *T* and high *f* region), a more pronounced linear relationship with *T* is observed, characterized by a reduction in the slope of linearity with increasing *f*. In addition, minor fluctuations in ReM are observable with incremental *T* changes. At lower frequencies, this behavior indicates

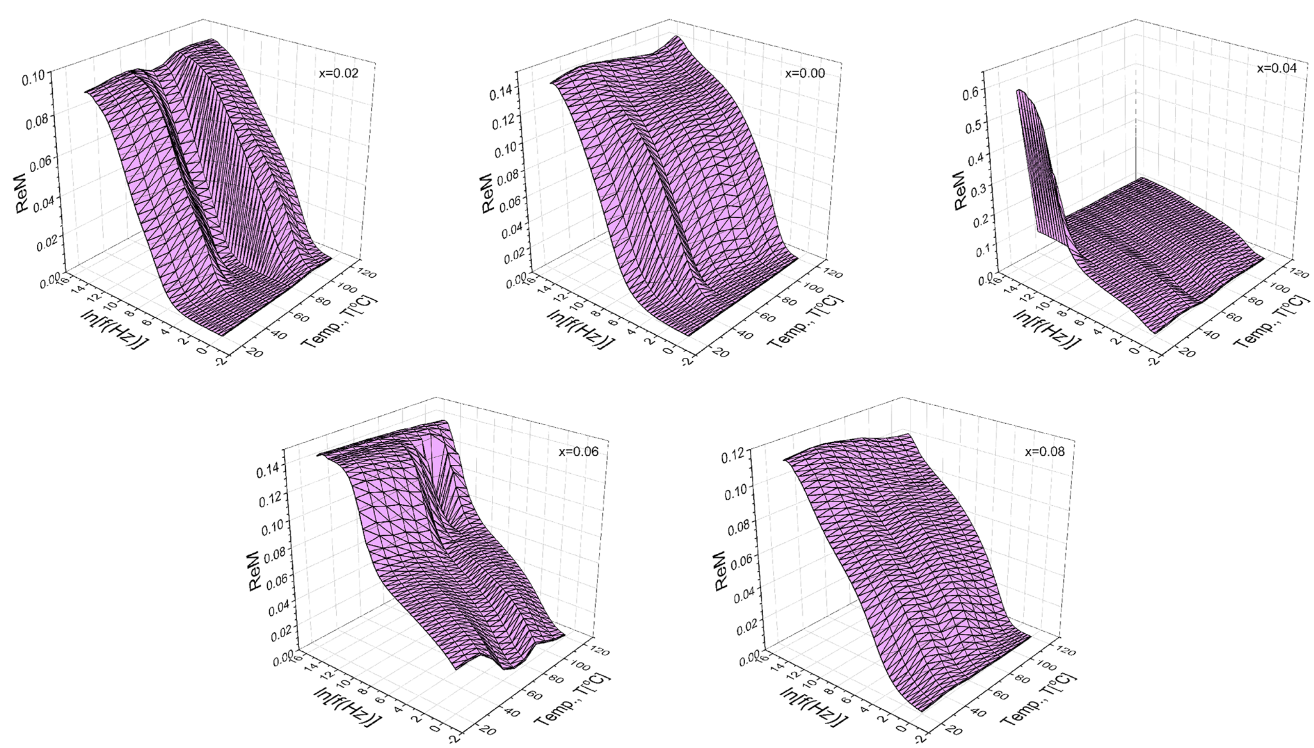

Fig. 10 3D representation of real modulus of H/S $Sr_{0.5}Ba_{0.5}Ho_xFe_{12-x}O_{19}$/NFO NCs

dispersion, where charge carriers can move between favorable hopping sites among ferrous (Fe^{2+}) and ferric (Fe^{3+}) ions. Such dispersive conductivity is typical in systems with mixed valence states, where charge carriers, usually electrons, hop between ions of different oxidation states, influenced by the availability of energetically favorable sites and the *f* of the applied external field.

3.2.6.2 Imaginary modulus (ImM) The ImM of H/S $Sr_{0.5}Ba_{0.5}Ho_xFe_{12\text{-}x}O_{19}$/NFO NCs is depicted in Fig. 11, illustrating the behavior across different Ho^{3+} ion substitution ratios as a function of *T*. Across all NCs, ImM initially rises, then decreases with increasing *f*, reaching a minimum before rising again, showing significant variation with *T*. Except for $x = 0.04$ NCs, where ImM peaks and then declines with increasing *f*, reaching a minimum. Fluctuations are evident along the *T* axis, particularly with a distinct valley at medium frequencies. However, for $x = 0.04$ NCs, the 3D ImM curves exhibit a distinctive pattern compared to other NCs, showing consistent and smooth variations across both *f* and *T*, with a noticeable spike at high frequencies around 20 °C. This indicates that the *ImM*, reflecting energy loss under an electric field, experiences rapid *f* -dependent changes within the grain boundaries. The presence of low and high peak values at approximately 5 Hz and 50 kHz for this substitution ratio suggests a transition from long-range to short-range mobility as *f* increases.

4 Conclusion

In this study, H/S $Sr_{0.5}Ba_{0.5}Ho_xFe_{12-x}O_{19}$/NFO NCs were successfully fabricated using the in situ sol–gel combustion method. XRD analysis confirmed the formation of a spinel cubic structure, while EDX monitoring ensured precise control over the chemical composition of the samples. A comprehensive investigation was conducted into the electrical and dielectric properties of these NCs, focusing on AC/DC conductivities, dielectric constants, dielectric loss, and dissipation factors. The study highlights several significant findings:

- *AC conductivity:* A strong dependency on frequency, temperature, and Ho-ion substitution ratio was observed, following a power law with an exponent near unity.
- *DC conductivity:* Distinct variations in DC conductivity were noted with increasing reciprocal thermal energy, indicating the effect of substitution ratios on conductivity.

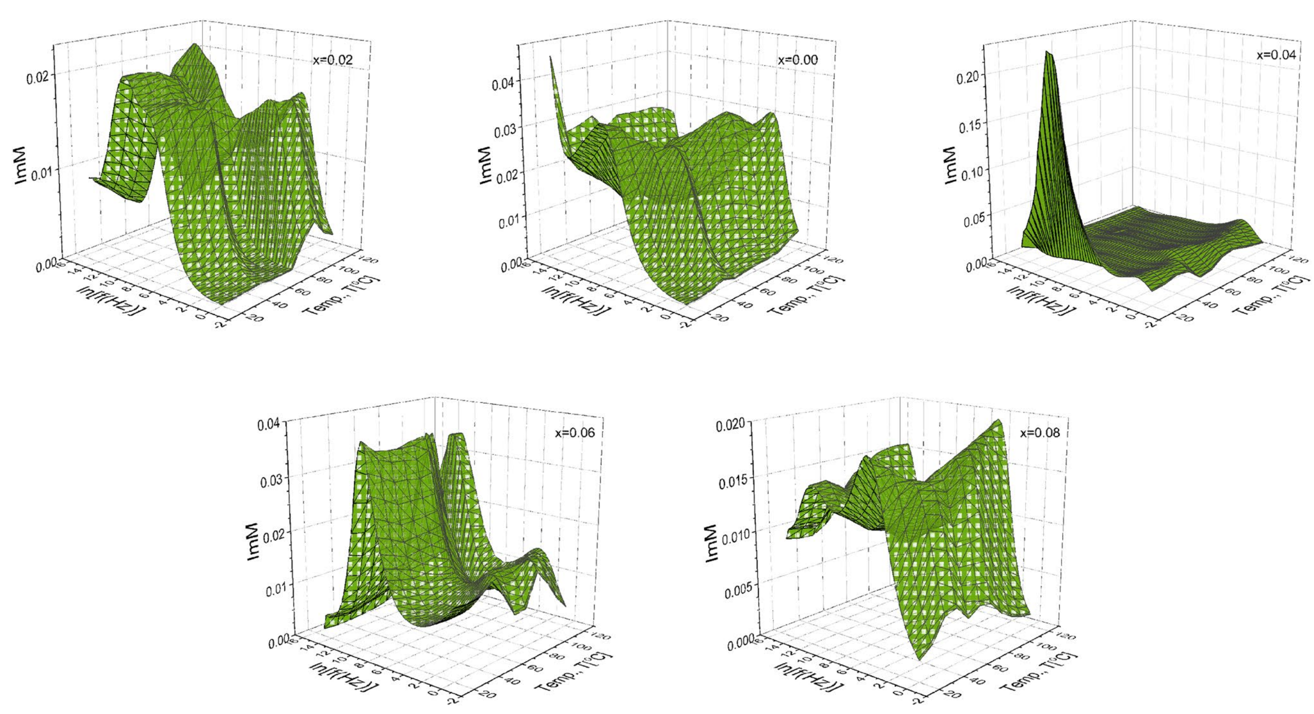

Fig. 11 3D representation of *ImM* of H/S $Sr_{0.5}Ba_{0.5}Ho_xFe_{12-x}O_{19}$/NFO NCs

- *Ho-ion substitution:* The variability in DC conductivity, characterized by activation energy, underscored transitional behaviors due to the substitution of Ho ions.
- *Dielectric properties:* Complex dependencies of the dielectric constant, dielectric loss, dissipation factor, and imaginary part of the modulus were identified, revealing changes in conduction mechanisms and energy loss dynamics under varying environmental conditions.
- *Environmental effects:* The analysis of electrical and dielectric properties across applied bias frequency and temperature measurements demonstrated a shift from long-range to short-range mobility, driven by both electronic and ionic processes.

This study provides valuable insights into the optimization of Ho-ion-substituted NCs, offering significant potential for their application in various advanced technological fields.

Acknowledgments

The authors acknowledge Institute for Research and Medical Consultations (IRMC) at Imam Abdulrahman Bin Faisal University (Saudi Arabia) for providing lab facilities.

Author contributions

B. Ünal: Formal analysis, data curation, writing—original draft, writing - review and editing. A. Baykal: supervision, conceptualization, writing—reviewing and editing, data curation. M.A. Almessiere: methodology, writing - original draft, conceptualization, project administration, writing—reviewing and editing. A. Manikandan: formal analysis, funding acquisition. Y. Slimani: formal analysis, data curation; writing—reviewing and editing. A. Ul-Hamid: resources.

Funding

No funding was received for this study.

Data availability

All data generated or analyzed during this study are included in this article. Additional data will be made available on request.

Declarations

Conflict of interest The authors declare that they have no known competing financial interests or personal relationships that could have appeared to influence the work reported in this paper.

Ethical approval This article does not contain any studies with human participants or animals performed by any of the authors.

References

1. R. Verma, M. Saini, A. Chauhan, R. Jasrotia, V. Dutta, S. Kharbanda, P. Thakur, B. Ravelo, P. Thakur, A.Thakur, Investigation of electrical, dielectric, magnetic and electrochemical characteristics of a BaFe12O19/Co0.5Zn0.5Fe2O4 nanocomposite. Physica B Condens. Matter **695**(15), 416600 (2024)
2. M. A. Siddiqui, M. Khalid, M. Younas, J. K. Khan, A. Ahmed, M.G.B. Ashiq, M. mana Al-Anazy, I. Boukhris, S. Ismail, K. Naz, Structural, dielectric and Magnetic properties of Samarium doped (Ni–Zn) based Spinel Ferrite ($Ni_{0.5}Zn_{0.5}Sm_xFe_{2-x}O_4$) nanomaterials. Ceram. Int. **50**(21), 43947(2024)
3. X. Xu, Y. Dong, Q. Hu, N. Si, C. Zhang, Electrochemical hydrogen storage materials: state-of-the-art and future perspectives. Energy Fuels **38**(9), 7579 (2024)
4. H. Liao, W. Zhong, C. Li, J. Han, X. Sun, X. Xia, T. Li, A. Noori, M.F. Mousavi, X. Liu, Y. Zhang, An intrinsically self-healing and anti-freezing molecular chains induced polyacrylamide-based hydrogel electrolytes for zinc manganese dioxide batteries. J. Energy Chem. **89**, 565 (2024)
5. K.A. Brown, S. Brittman, N. Maccaferri, D. Jariwala, U. Celano, Machine learning in nanoscience: big data at small scales. Nano Lett. **20**(1), 2–10 (2020)
6. S.E. Shirsath, M. Hussein, N. Assadi, J. Zhang, N. Kumar, A.S. Gaikwad, J. Yang, H.E. Maynard-Casely, Y.Y. Tay, J. Du, H. Wang, Y. Yao, Z. Chen, J. Zhang, S. Zhang, S. Li, D. Wang, Interface-driven multiferroicity in cubic $BaTiO_3$-$SrTiO_3$ nanocomposites. ACS Nano **16**(9), 15413–15424 (2022)

7. M. Chen, Y. Hao, C. Zhu, S. Liu, S. Liu, X. Hu, X. Li, H. Wu, X. Lu, J. Qu, Efficient exfoliation and dispersion of expanded graphite through dry ice explosion synergized shear flow field for high-thermal conductive NR/EG composite preparation in large-scale. Polymer **297**, 126854 (2024)
8. V.P. Phase, S.S. Kammar, C.S. Munnolli, Y.S. Madansure, A.A. Ibrahim, K.M. Batoo, R.H. Kadam, S.E. Shirsath, A.R. Shitre, Strain and exchange-spring mechanism of (1−x)Ni0.5Cu0.25Zn0.25Fe2O4 + (x)SrFe11Y1O19 magneticallysoft–hard ferrite composed nanoparticles. Part. Part. Syst. Charact. **41**, 2300225 (2024)
9. J. Xia, Y. Ning, Y. Luo, W. Chen, X. Wu, W. Wu, Q. Li, K. Li, Structural and magnetic properties of soft/hard NiFe2O4@SrCo0.2Fe11.8O19 core/shell composite prepared by the ball-milling-assisted ceramic process. J. Mater. Sci. Mater. Electron. **29**, 13903–13913 (2018)
10. S.F. Mansour, O.M. Hemeda, M.A. Abdo, W.A. Nada, Improvement on the magnetic and dielectric behavior of hard/soft ferrite nanocomposites. J. Mol. Struct. **1152**, 207 (2018)
11. S.T. Abarna, R.E. Vizhi, V. Harikrishnan, Examining the structural, magnetic and dielectric properties of exchange spring nanocomposite magnets comprising Ba0.5Sr0.5Fe12O19 and Zn0.5Co0.5Fe2O4. Results Phys. **48**, 106419 (2023)
12. M.A. Almessiere, B. Ünal, S. Ali, A. Baykal, Y. Slimani, A.V. Trukhanov, One-pot synthesis of hard/soft SrFe10O19/x(Ni0.8Zn0.2Fe1.8Cr0.2O4) nanocomposites: electrical features and reflection losses. Ceram. Int. **48**, 25390 (2022)
13. M.A. Almessiere, B. Ünal, A. Baykal, I. Auwal, Y. Slimani, A. Manikandan, A.V. Trukhanov, Investigation on electrical and dielectric properties of hard/soft spinel ferrite nanocomposites of CoFe2O4/(NiSc0.03Fe1.97O4)x. Vacuum **194**, 110628 (2021)
14. C. C. Chauhan, T.Gupta, S.S. Meena, M.F. Desimone, A. Das, C.S. Sandhu, K.R. Jotania, R.B. Jotania, Tailoring magnetic and dielectric properties of $SrFe_{12}O_{19}$/$NiFe_2O_4$ ferrite nanocomposites synthesized in presence of *Calotropis gigantea* (crown) flower extract. J. Alloys Compd. **900**,163415 (2022)
15. G. I. Choudhari, K. M. Kant, Structural, dielectric and magnetic properties of (100−x)SrFe12O19−(x)CoFe2O4 composites. J. Mol. Struct. **1311**(5), 138303 (2024)
16. M.A. Almessiere, B. Unal, I.A. Auwal, Y. Slimani, H. Aydin, A. Manikandan, A. Baykal, Impact of calcination temperature on electrical and dielectric properties of SrGa0.02Fe11.98O19/Zn0.5Ni0.5Fe2O4 hard/soft nanocomposites. J. Mater. Sci. Mater. Electron. **32**, 16589 (2021)
17. M. Kurian, D.S. Nair, Effect of preparation conditions on nickel zinc ferrite nanoparticles: a comparison between sol–gel auto combustion and co-precipitation methods. J. Saudi Chem. Soc. **20**(1), S517–S522 (2016)
18. S. Torkian, A.G. Reza, S. Razavi, Magnetic properties of hard-soft SrFe10Al2O19/Co0.8Ni0.2Fe2O4 ferrite synthesized by one-pot sol–gel auto-combustion. J. Magn. Magn. Mater. **416**, 408 (2016)
19. M.A. Almessiere, S. Caliskan, A. Baykal, D.S. Klygach, S.V. Trukhanov, Y. Slimani, T.I. Zubar, D.A. Vinnik, A.V. Trukhanov, E. Arslan, Impact of Ho substitution on structure, magnetic and electromagnetic properties hard-soft nanocomposites. Mater. Sci. Eng. B **308**, 117571 (2024)
20. J. Ferdaus, M.K. Das, A. Dey, B.C. Das, F. Alam, M. Rahaman, M.A. Hoque, M.S. Bashar, Influence of Zn-substitution on structural, magnetic, dielectric, and electric properties of Li–Ni–Cu ferrites. Heliyon **9**(11), e21633 (2023)
21. F. Alahmari, M.A. Almessiere, B. Ünal, Y. Slimani, A. Baykal, Electrical and optical properties of $Ni_{0.5}Co_{0.5\text{-}x}Cd_xNd_{0.02}Fe_{1.78}O_4$ ($x \leq 0.25$) spinel ferrite nanofibers. Ceram. Int. **46**, 24605 (2020)
22. C.G. Koops, On the dispersion of resistivity and dielectric constant of some semiconductors at audio frequencies. Phys. Rev. **83**, 121 (1951)
23. H. Sözeri, A. Baykal, B. Ünal, Low temperature synthesis of single domain Sr hexaferriteby solid state reaction route. Phys. Status Solidi A **209**, 2002 (2012)
24. Y. Slimani, N.A. Algarou, M.A. Almessiere, A. Sadaqat, M.G. Vakhitov, D.S. Klygach, D.I. Tishkevich, A.V. Trukhanov, S. Guner, A.S. Hakeem, A. Baykal, A. Manikandan, Fabrication of exchange coupled hard/soft magnetic nanocomposites: correlation between composition, magnetic, optical and microwave properties. Arabian J. Chem. **14**(3), 102992 (2021)

Publisher's Note Springer Nature remains neutral with regard to jurisdictional claims in published maps and institutional affiliations.